Journal of Materials Chemistry C

Accepted Manuscript

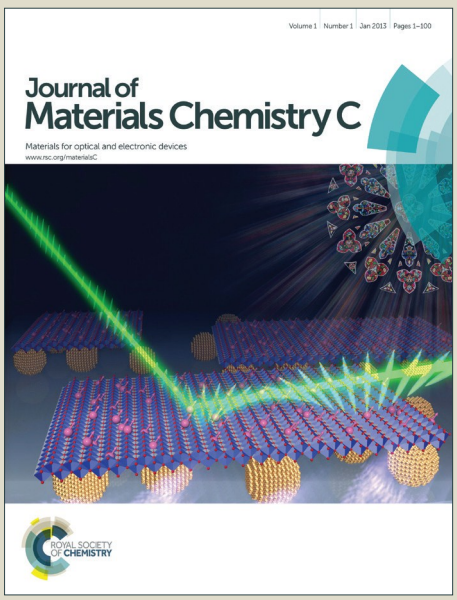

ROYAL SOCIETY OF CHEMISTRY

www.rsc.org/materialsC

The electronic and optical properties of novel germanene and antimonene heterostructure

Xianping Chen,*[abc†], Qun Yang,*[a†] Ruishen Meng,[a] Junke Jiang,[ab] Qiuhua Liang,[ab] Chunjian Tan,[bc] and Xiang Sun[bc]

[a]Faculty of Mechanical and Electrical Engineering, Guilin University of Electronic Technology, 541004 Guilin, China. E-mail: xianpingchen1979@126.com; qunyang1993@126.com

[b]Key Laboratory of Optoelectronic Technology & Systems, Education Ministry of China, Chongqing University, 400044 Chongqing, China.

[c]College of Optoelectronic Engineering, Chongqing University, 400044 Chongqing, China.

[†]These authors contributed equally to this work.

Abstract

In this work, the structural, electronic and optical properties of novel atomically thin systems based on germanene and antimonene nanocomposites have been investigated by means of density functional theory. We find that the germanene and antimonene monolayer are bounded to each other via orbital hybridization with enhanced binding strength. Most importantly, the band gap opening can be achieved. Our results demonstrate that AAII pattern has a direct band gap characteristic with a moderate value up to 391 meV, while the other three patterns have indirect band gaps tunable from 37 to 171 meV. Especially, changing the direction and strength of external electric field (E-field) can effectively tune the energy gap of germanene/antimonene bilayer in a wide range even with a semiconductor-metal transition. The work function of heterobilayer in AAII pattern which possesses a direct band gap nature can be tinkered up from -3.21 to 12.33 eV by applying different E-field intensities. In addition, the germanene/ antimonene bilayer exhibits more pronounced optical conductivity capability. The tunable bandgaps and work function together with superior visible light

response capability make the germanene/antimonene bilayer a viable candidate for optoelectronic applications.

1. Introduction

Ever since its experimental realization in 2004,[1] graphene, a flat monolayer of carbon atoms tightly packed into a two-dimensional (2D) honeycomb lattice, has emerged as a candidate for future electronics applications because of its extraordinary electronic and mechanical properties.[2-5] Inspired by the discovery of graphene, both experimental and theoretical researchers focus their research interests on the members of group-V elemental 2D atomic-layer systems including silicene, germanene, and stanene. Compared with their bulk form, those 2D materials exhibit so many unusual properties,[6-8] such as high charge-carrier mobility, outstanding mechanical performance, and large surface-to volume ratio. However, the intrinsic shortcoming of these group-IV 2D materials is gapless which gives rise to their poor performance in the FET applications. To our best knowledge, the key to develop 2D material-based electronics urgently lies in opening a tunable band gap of it. To achieve this, an alternative route is the realization of heterostructures. Many strategies have been conducted for band gap engineering of graphene and silicene.[9-14] However, there are still little efforts have been paid to open the band gap of germanene by heterostructures. The reasons can be divided into two parts: (i) Most recently, germanene was successfully grown on Pt(111),[15] thus, we note that the germanene-based electronics are still in the early exploration stages and much work is needed. (ii) Because of its buckled honeycomb structure and the existence of dangling bonds, free standing germanene exhibits a significantly high chemical reactivity which endows itself susceptible to the substrate.[16] Therefore, it is still desirable to find a proper nanostructure to accommodate germanene with small lattice mismatch and open the band gap of germanene.

Most recently, Zhang *et al.*[17] theoretically identified two novel mono-elemental thin films with high stability and a suitable wide band gap, namely, the arsenene (As monolayer) and antimonene (Sb monolayer), which triggers an upsurge of further theoretical investigation of its other unique properties,[18-20] for example, Liang *et al.*[21] demonstrated that the antimonene

can be transited from trivial insulator to topological insulators by applying biaxial tensile strain. The antimonene nanosheets have a different buckling structure from the single layer of phosphorus called phosphorene, which prefer to the blue-phosphorus-like structure rather than the black-phosphorus one. In this work, electronic structures and optical properties of germanene/antimonene (Ge/Sb) nanocomposites have been investigated *via* first principles calculations. We systematically calculated and analysed the different stacking orders, band structures, binding energies, charge density difference, PDOSs, work functions and optical properties of the composites. We also calculated the E_g, and work function of composite under different external electric field (E-field). Most interestingly, the band gap opening of the hybrid system is observed even without considering the spin orbital effects (SOC), and the applied E-field has a substantial effect on the band gap of hetero-bilayer. Besides, the work function of heterobilayer in AAII pattern can be tinkered up from -3.21 to 12.33 eV by applying an E-field with various intensities. The real part of the optical conductivity exhibits an enhancement peak in the visible light region compared to the simplex germanene and antimonene monolayer. We firmly believed that the excellent properties we obtained from Ge/Sb bilayer will inspire the experimenter to realize the Ge/Sb nano-composites in the future.

2. Computational methods

In our work, all the structural relaxation and electronic calculations were carried out by first-principles calculations based on the DFT using the DMol^3 code[22] of Materials Studio. The generalized gradient approximation (GGA) with Perdew-Burke-Ernzerhof (PBE) exchange-correlation functional[23] was used to describe the exchange-correlation interaction. Moreover, to take the van der Waals (vdW) into consideration, DFT-D (D stands for dispersion) method Grimme[24] was employed due to the weak interactions are not well described by the standard PBE functional.[8, 25-27] Besides, double numerical atomic orbital plus polarization (DNP) was chosen as the basis set. The global orbital cutoff was set to be 5.0 Å, and a supercell with the 20 Å vacuum layer was utilized to prevent the interactions between neighbouring layers in the direction normal to the antimonene and germanene surfaces. The K

points of 16×16×1 was set for the geometry optimization and 20×20×1 for accurate electric characteristics calculations, respectively. All the lattice constants and atom coordinates were relaxed until the convergence of the force on each atom within 0.01 eV/A˚. The optical properties were calculated in CASTEP code[28] with a plane-wave kinetic energy cutoff of 500 eV, and the K point mesh was set to 8×8×1 considering the limited computational resources.

Concerning the energetics of the heterostructures, the binding energy (E_b) per atom is summarized in Table 1 which can be defined as,

$$E_b=[E_{total}-(E_{antimonene}-E_{germanene})]/N \quad (1)$$

where E_{total}, $E_{antimonene}$ and $E_{germanene}$ represent the total energy of the composite, isolated antimonene and germanene, respectively, and N corresponds to the total number of Ge atom in the unit cell. A negative E_b corresponds to a stable adsorption structure.

3. Results and discussion

The lattice constant, buckling height and the Ge-Ge bond length of the germanene after the geometry optimization in our calculation are 4.02 Å, 0.691 Å and 2.422 Å respectively, which agree well with the reported values of 4.061 Å, 0.690 Å and 2.444 Å.[29] Our optimized lattice constant for antimonene monolayer is 4.08 Å, which is slightly larger than the previous calculated value of 3.94 Å.[17] The unit cell of our system is composed by 2×2 unit cells for both germanene and antimonene monolayer leading to a lattice mismatch of around 1.47%. Compared with the hybrid systems investigated previously,[11, 12,13, 30] the present lattice mismatch values are very small. It should be pointed out that, the electronic properties of antimonene is vulnerable to the strain, while germanene is resistant to strain. To compensate the lattice mismatch between germanene and antimonene, we chose to keep the antimonene lattice fixed, and stretched the germanene system. The elongation of the lattice constant in germanene lattice is around 1.47%, and no significant changes were observed in its electronic structure because the sublattice symmetry was still maintained. Thus, the lattice constant of germanene was set to match to that of the antimonene monolayer in the supercell. Both the lattice constants and the atomic geometry of supercells are then

fully relaxed. The mismatch will finally disappear, leading to the commensurate systems.

The 2D Ge/Sb bilayer was constructed by hybridizing germanene with antimonene monolayer, and we took four representative configurations into account, namely, AAI-, AAII-, ABI-, and ABII-stacking. The corresponding fully optimized geometric structures are shown in Fig. 1. For AA-stacking (see Fig. 1(a) and (b)), germanene and antimonene monolayers are matched perfectly without mismatch in the xy plane, whereas for AB-stacking (see Fig. 1(c) and (d)), one Sb atom in the supercell was set to sit on the hollow site above the center of a hexagon of germanene. Pattern II including AAII and ABII we obtained is flip the germanene of pattern I vertically 180º, which leads to a novel heterostructure different from pattern I. The computed structural and electrical characteristic parameters are listed in Table 1, where one can see that the buckling height of the germanene ($\delta_{\text{Ge-Ge}}$) and antimonene ($\delta_{\text{Sb-Sb}}$) layer in all patterns have a significant increase in comparison with initial values of 0.691 Å and 1.696 Å. The binding energy (E_b) of the bilayers vary from -166 meV to -283 meV per atom with four different stacking orders, the interlayer distance d follows the order of ABI (2.594 Å) < ABII (2.806 Å) < AAII (2.868 Å) <AAI (3.093 Å), which corresponds to the E_b. Although ABI-stacking has the shortest interlayer distance of 2.594 Å, which is within the range of the sum of the covalent radii of the Ge and Sb atom (2.61 Å),[31] but the ABI pattern has staggered stacking, the shortest distance between Ge atom of germanene and Sb atom of antimonene is 3.494 Å which is greatly larger than the bonding distance, indicating the absence of Ge-Sb covalent bonds in the hybrid structures. What's more, the calculated binding energies per Ge atom is up to 283 meV, which is significantly higher than the binding energies of the weak vdW interactions, suggesting that the germanene and antimonene are bounded to each other *via* other mechanism, for example, orbital hybridization or electrostatic interaction.[32] To put it another way, from Table 1 we can obtain that ABI-stacking is the energetically favourable pattern with the lowest binding energies and the shortest interlayer distance, while AAII-stacking possesses the highest Mulliken charge transfer (ΔQ) and the largest band gap (E_g). Besides, from the view of energy, although the ABII pattern is less stable than ABI pattern, it is more energetically favourable than AAII one. So in the following calculations, we mainly focus on ABI-, ABII- and AAII-stacking.

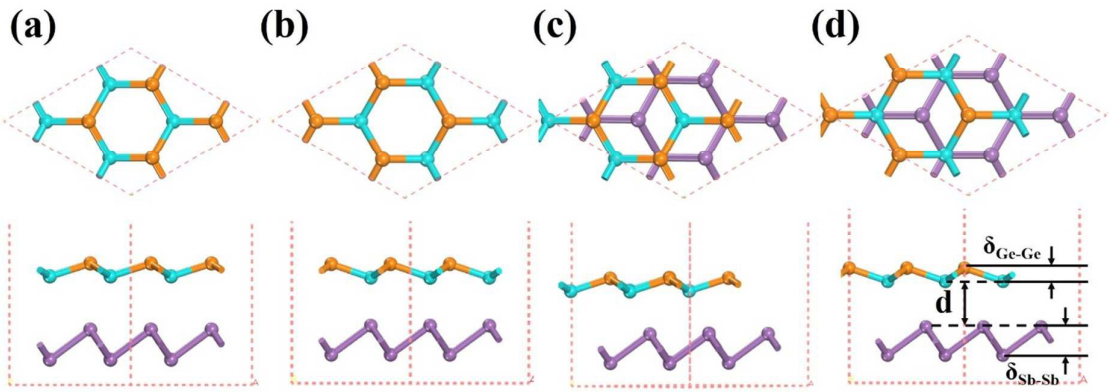

Fig. 1. Top and side view of the atomic model of the Ge/Sb heterobilayer: (a) Pattern AAI, (b) Pattern AAII, (c) Pattern ABI, (d) Pattern ABII. The "*d*" in pattern ABII denotes interlayer distance. $\delta_{Ge\text{-}Ge}$, $\delta_{Sb\text{-}Sb}$ are the buckling height of the germanene and antimonene layer respectively. The Sb atom of the antimonene, and the Ge atoms in upper/lower level are represented by purple, yellow and bule balls respectively. The unit cells are shown in red dashed lines.

Table 1 Structure/electronic properties of Ge/Sb with different patterns, including the distance between the lower Ge atom to the upper animonene plane (*d*), amplitude of the buckling of the Ge ($\delta_{Ge\text{-}Ge}$) and Sb superlattice ($\delta_{Sb\text{-}Sb}$), binding energy (E_b), Mulliken charge transfer (Q) and energy band gap (E_g). The negative signs donote that the charges transfer from antimonene to germanene.

Pattern	*d* (Å)	E_b (meV)	ΔQ (e)	E_g (meV)	$\delta_{Ge\text{-}Ge}$ (Å)	$\delta_{Sb\text{-}Sb}$ (Å)
AAI	3.093	-166	-0.076	171	0.734	1.722
AAII	2.868	-208	-0.392	391	0.792	1.711
ABI	2.594	-283	-0.176	60	0.747	1.713
ABII	2.806	-233	-0.024	37	0.713	1.718

The band structures of the optimized free-standing germanene and antimonene are given in Fig. 2(a) and (b) respectively. For pristine germanene, the filled-state π and empty state π^* bands of it touch each other at the high-symmetry K point (Dirac point) of the Brillouin zone (BZ) in the case of without considering the spin orbital coulping (SOC) effect, resulting in the

gapless semi-metallic nature. While the freestanding antimonene monolayer is an indirect semi-conductor with a wide band gap of 1.245 eV, the valence band maximum (VBM) and conduction band minimum (CBM) are located at Γ point and K point respectively. Zhang *et al.*[17] have shown that the band gap of antimonene monolayer is 1.77 eV with two highest valence bands degenerated at the Γ point through the use of CASTEP code with GGA/PBE level. The band structure we obtained is similar to their results only with the band gap value smaller than the value they calculated. Such discrepancy is believed to be caused by different modules of the software package we used. In order to verify the model and the computation methods, the band structure of antimonene monolayer is also reproduced by using CASTEP code with GGA/PBE level. The band gap of antimonene we obtained is 1.753 eV (Supporting Information, Fig. S1), which is in reasonable agreement with the reported values of 1.77 eV predicted by Zhang *et al.*[17] with GGA/PBE function. Compared with the calculation by Liang *et al*.[21] in which the VBM appears at the Γ point while the CBM locates at about the middle point of ΓM. Furthermore, their result shows that these two bands are obviously splitted, as a consequence, the band gap of antimonene is calculated to be 1.52 eV. We consider the discrepancy is mainly because of the effect of SOC. Surprisingly, when the hybrid Ge/Sb structure is taken shaped, the interaction between bilayer gives rise to the open of indirect band gap of 60 meV and direct band gap of 391 meV for the ABI-stacking and AAII-stacking respectively. As can be seen in Fig. 2(c), (d) and (e), the CBM of the ABI configuration still locates at the K point of the BZ, while the VBM shifts to the middle of the ΓK point. For ABII pattern, the CBM is still located at K point, whereas the VBM lies Γ point of BZ. For the case of AAII pattern, both the CBM and VBM locate at the K point similar to the pristine germanene.

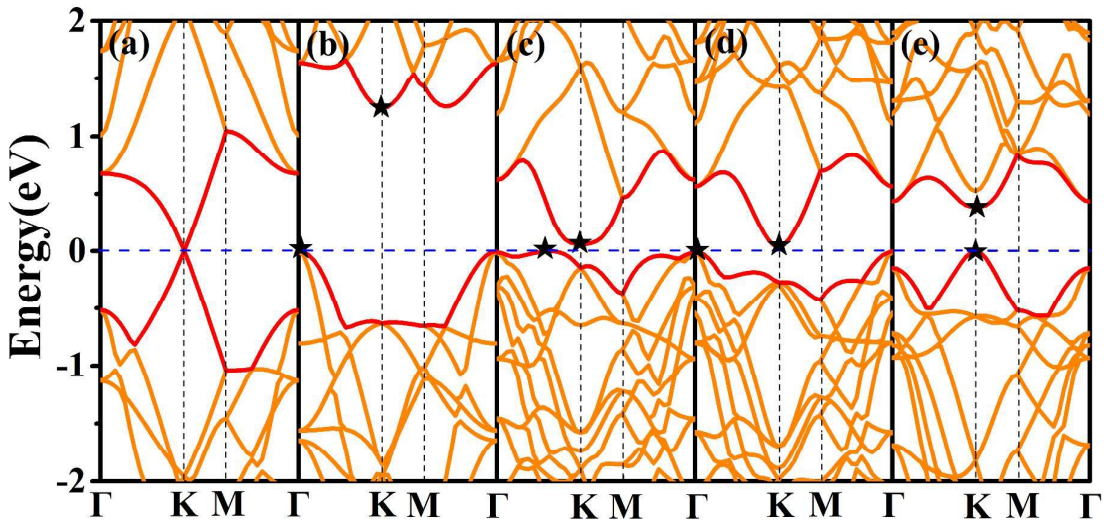

Fig. 2. The band structures of (a) pristine germanene, (b) pristine antimonene, (c) ABI pattern of Ge/Sb bilayer, (d) ABII pattern and (e) AAII pattern of heterobilayer. The CBM and VBM are marked with black stars and the Fermi level is set at 0 eV and represented by bule dashed line.

In order to explore the mechanism of the interaction between germanene and antimonene, the total and atom projected density of states (PDOS) of ABI, ABII and the AAII configuration of heterobilayer are plotted in Fig. 3. For the case of ABI-stacking, it can be seen clearly that the line shape and the intensity of peaks of PDOS for separated antimonene is similar to that of heterobilayer system, which indicates that the antimonene dominates the electronic properties of composites, besides, the Ge d and Sb d orbitals are almost fully overlapped in the whole range of energy, indicating the presence of orbital hybridization. As displayed in Fig. 3, the PDOS of ABII-stacking is almost identical with ABI-stacking except for slight changes near the Fermi level with a minor downward movement of PDOS. For AAII-stacking, the electronic states in the characteristic peak in the valence band (-1 to 0 eV) of the heterobilayer are contributed by the germanene, while the peaks on the conduction band (0 to 3 eV) are mainly dominated by antimonene. Both of them are dominated by their p orbitals. Furthermore, the Ge p and Sb p, Ge p and Sb d orbitals share the similar states within the range of -2 to 3 eV and 0 to 3 eV respectively, indicating the

existence of orbital hybridization. Therefore, we get the conclusion that the germanene and antimonene are bounded to each other *via* orbital hybridization, which is the reason for high binding energies. The mechanism of interaction between two considered monolayers can be understood.

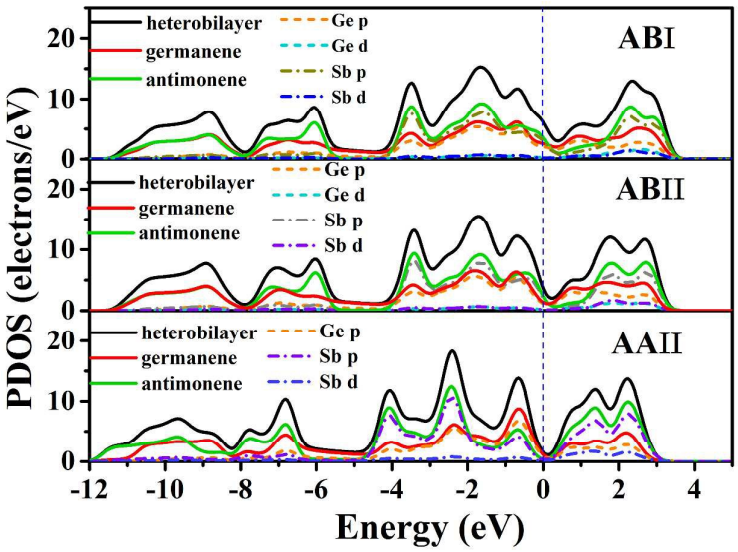

Fig. 3. The density of states for the ABI pattern (upper), ABII pattern (middle) and the AAII pattern (bottom). The Fermi level is represented by bule dashed line.

Towards a better understanding on the strong interaction between germanene and antimonene layers, the charge density difference (CDD) of the ABI-stacking, ABII-stacking and the AAII-stacking for Ge/Sb heterobilayer are calculated, which can be expressed as:

$$\Delta\rho = \rho_{\text{total}} - \rho_{\text{germanene}} - \rho_{\text{antimonene}} \quad (2)$$

where ρ_{total}, $\rho_{\text{germanene}}$, $\rho_{\text{antimonene}}$ are the total charge densities of the heterobilayer, isolated germanene, and antimonene monolayer in the corresponding heterobilayer system respectively. As shown in Fig. 4, the yellow and blue colors represent charge depletion and accumulation, respectively. It is shown that for ABI-stacking, the electrons are depleted on the upper Sb atoms and lower Ge atoms, while some of them are accumulated at the interlayer region. For ABII-stacking, a small amount of

electrons are depleted on the upper Sb atoms and lower Ge atoms which agrees with the fact that small charges (0.024 |*e*|) transfers from antimonene to germanene. For the case of AAII-stacking, the ranges of charge redistributions is much wider as compared to the ABI-stacking, it is of significance to find that the evident charge rearrangement localized at the interlayer region, which is the result of the orbital overlaps. In addition, the electrons are depleted on the upper Sb atoms and lower Ge atoms while the majority of them are accumulated at interlayer region and upper Ge atoms, such apparent charge redistributions in the AAII-stacking are consistent with the large charge transfer which is listed in Table 1, the large charges (0.392 |*e*|) transferring from antimonene to germanene significantly modify the electronic property of germanene, leading to a wide direct band gap of 0.391 eV. In addition, for AAII pattern, the distinct charge redistributions at the interfacial region in combination with the interlayer distance of 2.868 Å which close to the Ge-Sb bonding distance indicate some weak bonds may be formed between germanene and antimonene monolayer. Nowadays, Quantum Chemical Topology (QCT)[33] method based on the topological analysis of the electron localization function (ELF)[34, 35] has been widely introduced for modern bond analysis.[36-38] To get a further insight into the nature of bonding between the germanene and antimone layer, the ELF of AAII pattern is analysed by means of QCT. The Mulliken charge analysis shows that the charge transfer of ABI pattern is up to 0.176 |*e*|, therefore, we calculate the ELF of ABI pattern. As shown in Fig. 5(a), the ELF for ABI pattern is close to zero in the interlayer region, thus, it is incapable of chemical bond forming between the germanene and antimonene. By contrast, the ELF for AAII pattern is

close to one in the interlayer regions indicating the electrons are paired to form covalent bonds between Ge and Sb atoms (see Fig. 5(b)). Such phenomenon is absent for ABI pattern. Therefore, we come into the conclusion that there are some covalent bonds formed between germanene and antimonene in AAII pattern.

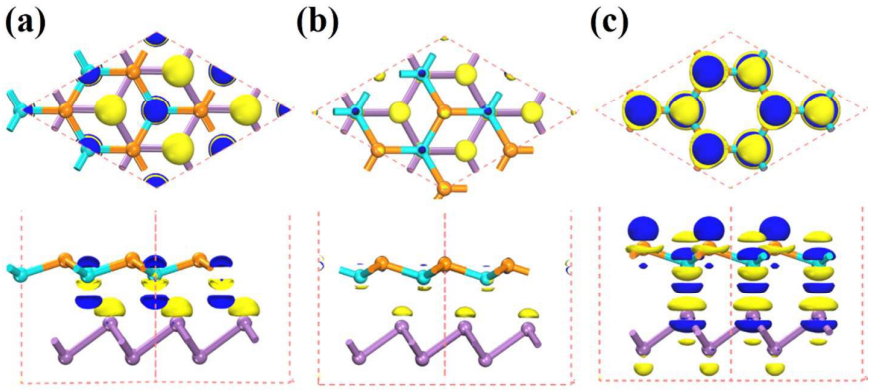

Fig. 4. The charge density difference of the (a) ABI pattern (b) ABII pattern and (c) AAII pattern. Blue and yellow represent charge accumulation and depletion respectively. The isovalue is set to be 0.008 e/Å^3.

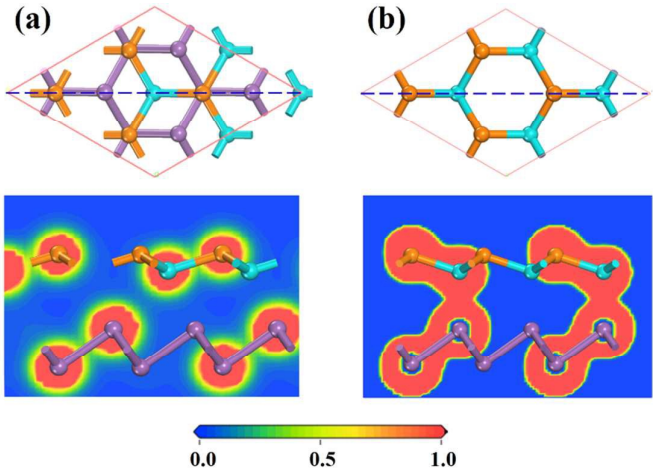

Fig. 5. ELF contour plots for the (a) ABI pattern and (b) AAII pattern. Red (blue) regions correspond to large (small) ELF values.

Applying external E-field has been recognized as one of the efficient methods to get a tunable band gap.[39-43] Thus, in this section, we mainly investigate the effect of E-field on the electronic properties of the germanene/antimonene compostites in ABI-stacking, ABII-stacking and AAII-stacking. The computed energy gap values as a function of external E-field is displayed in Fig. 6. The positive direction of the E-Field is shown in the inset of Fig. 6. As shown in Fig. 2, ABI and ABII patterns have indirect band gap natures, while the AAII pattern has a direct energy band gap feature. It is of interest to note that the band gap natures of all those three patterns are completely independent of the external E-field. When applied a negative external E-field on ABI pattern, the band gap increases to the maximum value of 300 meV at a very tiny intensity of ~ -0.003 a.u (1 a.u.=51.36 V/Å), further increasing the intensity of negative external E-field will reduce the bandgap till disappears under E-field not beyond -0.01 a.u. When a positive external E-field is applied on ABI pattern, E_g reduces to zero rapidly and correspondingly causes a semiconductor−metal transition. The similar tendency of the change of band gap values under different electric field is found in ABII pattern. For the case of AAII pattern, under a positive external E-field, E_g first increases with the increase of the E-field because the lowest conduction band will shift up and penetrates the E_F. In addition, we observe that the applied electric field has a substantial effect on the conduction band and valence band near the K point and Γ point. When the E-field intensity reaches 0.003 a.u, the conduction band at K point shifts up and the valence band at K point shifts down, furthermore, both the conduction band and valence band at Γ point shift up. As a result, the CBM and VBM shift from K point to Γ point of the BZ with the maximum band gap of 680 meV, which is shown on the right side of the Fig. 6. It is also believed that the band gap can be further enlarged if we take the SOC effect into account. When the strength of the E-field is further increased, the band gap value will decrease then vanishes at the E-field intensity of 0.009 a.u, a semiconductor–metal transition occurs. We have also displayed the variation of the electronic band structure of germanene/antimonene heterobilayer in AAII pattern upon different electric fields in the Supplementary Information (Fig. S1).

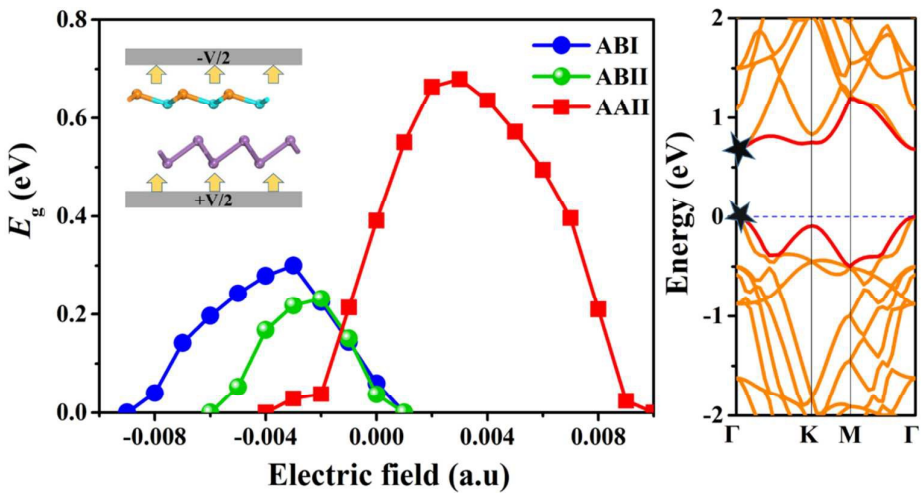

Fig. 6. The calculated energy band gap as a function of E-field for ABI pattern, ABII pattern and AAII pattern, the filled squares and filled circles represent the direct band gap and indirect band gap value respectivity. (Upper inset) The positive direction of the E-field is pointed by the yellow arrows from antimonene to germanene. (Right) The band structure of AAII pattern at the E-field of 0.003 a.u

The work function of graphene is a significant parameter in controlling the field-emission properties of graphene-based electronics devices. Previous experiment studies exhibit that the work function of graphene depends sensitively on the numbers of layers[44], chemical doping[45] and external electrical field.[46] Inspired by those researches, the work functions of the Ge/Sb bilayer under different strength of E-field are calculated to explore its possible application in the field emission devices. We choose AAII-stacking of Ge/Sb bilayer as a research object because the tunable direct band gap nature makes it more suitable for the application in optoelectronic devices. The calculated work function of germanene is 4.57 eV, which is slightly larger than the previously theoretical calculation because of different software we used, the value we obtained is comparable to the work function of graphene.[46,47] In addition, the calculated work function of antimonene is 4.76 eV. After the considered two monolayers are paired together in AAI-stacking, the obtained work function of composite is 4.49 eV

which is lower than that of individual germanene and antimonene. Fig. 7 shows the work functions of Ge/Sb heterobilayer in AAII-stacking as a function of the E-Field, from which we can get the conclusion that the work function of Ge/Sb bilayer is a linear function of the external E-field strength and has a wide controllable range. Our results indicate that the work function of Ge/Sb composite can be tuned from -3.21 eV to 12.33 eV within E-field strength range from 0.01 a.u to -0.01 a.u. To our best knowledge, one cannot increase the E-field intensity arbitrarily because the strong E-field could destroy the stable structure of the Ge/Sb heterobilayer, resulting in a crack of the chemical bonds. The E-field intensity we used is not enough to destroy the stable structure of the heterobilayer, thus, we predict that the work function of Ge/Sb composite can be adjusted to a wider range in experiment when a stronger E-field is applied. In a word, this wide range of adjustable work function enables the Ge/Sb bilayer to be a suitable material for field-emitted devices.

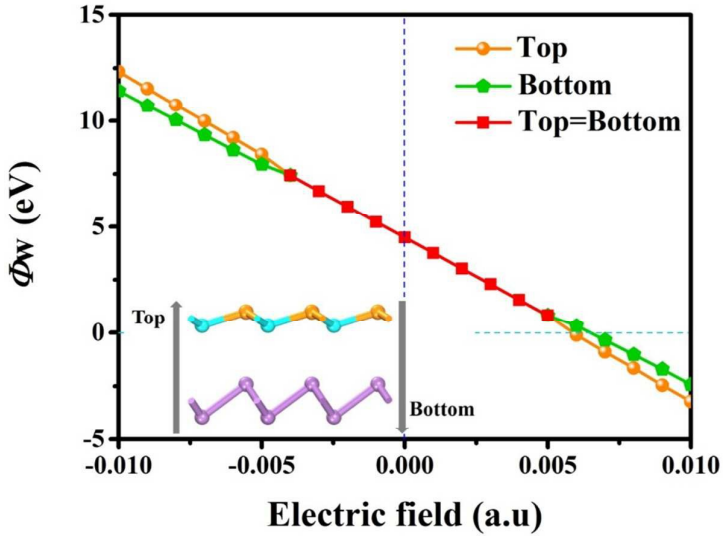

Fig. 7. The calculated work function of the AAII pattern as a function of E-field strength in directions with top and bottom. The horizontal and vertical dash lines were set as the datum line of work function and E-field strength in value zero, respectively.

The optical conductivity can be used to characterize the optical properties of any system containing 2D sheets.[48] In this section, the optical properties of the Ge/Sb bilayers in ABI-stacking, ABII-stacking and AAII-stacking are discussed on the basis

of the optical conductivity, as shown in Fig. 8. First, we discuss the optical conductivity of the individual germanene, the first peak in Re $\sigma_{2D}(\omega)$ of germanene near 1.8 eV is a consequence of 2D saddle points in the $\pi^*-\pi$ interband structure located at the six M points at the BZ boundary, while the higher peaks near 3.7/4.1 eV are ascribed to $\sigma\rightarrow\sigma^*$ transitions mainly at the Γ point of the 2D BZ. These peaks we obtained are slightly red-shifted in comparison to the previously theoretical study which reported the peaks located at 2.0 eV, 4.0 eV and 4.7 eV respectively.[49] For antimonene monolayer, it exhibits a prominent peak in the visible light range (2.8-3.19 eV) and UV range (> 3.19 eV). When the heterostructure is formed, the obvious changes of optical conductivity that indeed are worthy of exploration. For the case of AAII pattern, the peaks in the range of 2.8 to 3.8 eV are slightly weakened with respect to the pure antimonene but much higher than that of individual germenene monolayer. In contrast to the AAII pattern case, the ABI pattern displays a more distinct change of optical conductivity, it possesses a relatively stronger peak in the visible light range (1.64-3.19 eV) than that of the two pristine monolayers and AAII pattern, moreover, it exhibits considerable conductivity index in the infrared light zone (< 1.64 eV) and ultraviolet light region (> 3.19 eV). For ABII pattern, which can be seen as the entire spectrum is blue-shifted and moved down in comparison with ABI pattern. From the analysis of the optical conductivity above, it leads us to conclude that the strain induced by placing one monolayer on top of the other will alter the optical properties. Concomitantly, the Ge/Sb heterobilayer in most energetically favourable pattern presents an evident enhancement of photoresponse under the visible light irradiation, which shows their potential in photo-related application prospect.

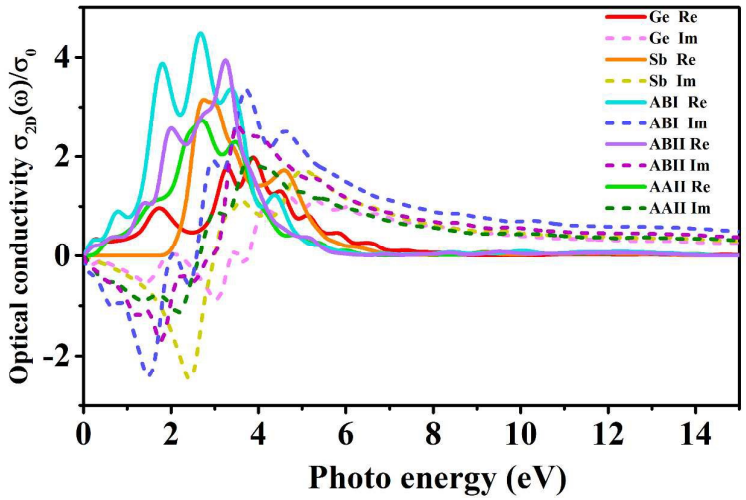

Fig. 8. Optical conductivity in units of the ac conductivity σ_0 of germanene, antimonene, ABI pattern, ABII pattern and AAII pattern. Real part: solid line, imaginary part: dotted line.

4. Conclusions

In summary, the structural, electronic and optical properties of the novel atomically thin systems based on germanene and antimonene are carefully investigated through first principles calculations based on DFT-D. Our calculations show that the germanene and antimonene are bounded to each other *via* orbital hybridization caused by the chemically active germenene layer, leading to the improvement of stability of the hybrids. As a result, the four representative stacking patterns are all stable without chemical bonds formed except for AAII pattern, the binding energies of four different stacking patterns range from -283 meV (ABI-stacked) to -166 meV (AAI-stacked). Due to the interlayer charges redistribution, a sizable gap is opened at the Dirac point of germanene. Besides, the introduction of the external E-field has a remarkable effect on the band gap modification, the indirect band gap of ABI and ABII pattern can be tuned from 0 to 300 meV and 0 to 232 meV, respectively, while the direct band gap of AAII pattern can be modulated from 0 to 680 meV. This unique and tunable band gap of Ge/Sb bilayer implicates the applications on the high performance nano-electronic devices. Furthermore, the calculated work function of the bilayer is 4.49 eV, lower than the individual considered monolayer, and it can be modulated in a wide range by

applying E-field with various intensities, indicating that the Ge/Sb heterobilayer materials are very promising for field-emitted devices. For optical properties, the most energetically favourable structure shows enhanced optical conductivity in the visible light region, this superior optical property indicates the potential of the Ge/Sb heterostructure in the photoelectric devices. With the excellent electronic and optical properties combined, 2D Ge/Sb composites are expected to be with a great potential in nanoelectronic applications.

Acknowledgements

The research is co-supported by the National Natural Science Foundation of China under Grant No. 51303033 and the Guangxi Natural Science Foundation under Grant No. 2014 GXNSFCB118004.

Notes and references

1. K. S. Novoselov, A. K. Geim, S. Morozov, D. Jiang, Y. Zhang, S. a. Dubonos, I. Grigorieva and A. Firsov, *science*, 2004, **306**, 666-669.
2. K. Novoselov, A. K. Geim, S. Morozov, D. Jiang, M. Katsnelson, I. Grigorieva, S. Dubonos and A. Firsov, *nature*, 2005, **438**, 197-200.
3. F. Schedin, A. Geim, S. Morozov, E. Hill, P. Blake, M. Katsnelson and K. Novoselov, *Nature materials*, 2007, **6**, 652-655.
4. A. K. Geim and K. S. Novoselov, *Nature materials*, 2007, **6**, 183-191.
5. S. Morozov, K. Novoselov, M. Katsnelson, F. Schedin, D. Elias, J. Jaszczak and A. Geim, *Physical review letters*, 2008, **100**, 016602.
6. S. Cahangirov, M. Topsakal, E. Aktürk, H. Şahin and S. Ciraci, *Physical review letters*, 2009, **102**, 236804.
7. H. Şahin, S. Cahangirov, M. Topsakal, E. Bekaroglu, E. Akturk, R. T. Senger and S. Ciraci, *Physical Review B*, 2009, **80**, 155453.
8. X.-P. Chen, N. Yang, J.-M. Ni, M. Cai, H.-Y. Ye, C. K. Wong, S. Y. Leung and T.-L. Ren, *Electron Device Letters, IEEE*, 2015, **36**, 1366-1368.
9. W. Geng, X. Zhao, H. Liu and X. Yao, *The Journal of Physical Chemistry C*, 2013, **117**, 10536-10544.
10. J. Zhu and U. Schwingenschlögl, *Journal of Materials Chemistry C*, 2015, **3**, 3946-3953.
11. Y. Ding and Y. Wang, *Applied Physics Letters*, 2013, **103**, 043114.
12. Y. Ma, Y. Dai, M. Guo, C. Niu and B. Huang, *Nanoscale*, 2011, **3**, 3883-3887.

13. M. Houssa, B. van den Broek, E. Scalise, G. Pourtois, V. Afanas' ev and A. Stesmans, *Physical Chemistry Chemical Physics*, 2013, **15**, 3702-3705.
14. L. Sheng-Shi, Z. Chang-Wen, J. Wei-Xiao, L. Feng and W. Pei-Ji, *Physical Chemistry Chemical Physics*, 2014, **16**, 22861-22866.
15. L. Li, S. Z. Lu, J. Pan, Z. Qin, Y. Q. Wang, Y. Wang, G. Y. Cao, S. Du and H. J. Gao, *Advanced Materials*, 2014, **26**, 4820-4824.
16. K. Yang, S. Cahangirov, A. Cantarero, A. Rubio and R. D'Agosta, *Phys.rev.b*, 2014, **89**, 182-187.
17. S. Zhang, Z. Yan, Y. Li, Z. Chen and H. Zeng, *Angewandte Chemie International Edition*, 2015, **54**, 3112-3115.
18. S. Zhang, Y. Hu, Z. Hu, B. Cai and H. Zeng, *Applied Physics Letters*, 2015, **107**, 022102.
19. C. Xia, B. Xue, T. Wang, Y. Peng and Y. Jia, *Applied Physics Letters*, 2015, **107**, 193107.
20. Y. Wang and Y. Ding, *Physical Chemistry Chemical Physics*, 2015, **17**.
21. J. Liang, L. Cheng, J. Zhang and H. Liu, *arXiv preprint arXiv:1502.01610*, 2015.
22. B. Delley, *The Journal of chemical physics*, 2000, **113**, 7756-7764.
23. J. P. Perdew, K. Burke and M. Ernzerhof, *Physical review letters*, 1996, **77**, 3865.
24. S. Grimme, *Journal of computational chemistry*, 2006, **27**, 1787-1799.
25. X.-P. Chen, N. Yang, J.-K. Jiang, Q.-H. Liang, D.-G. Yang, G.-Q. Zhang and T.-L. Ren, *Electron Device Letters, IEEE*, 2015, **36**, 606-608.
26. Q. Yang, R. Meng, J. Jiang, Q. Liang, C. Tan, M. Cai, X. Sun, D.-G. Yang, T.-L. Ren and X. Chen.
27. X. Chen, J. Jiang, Q. Liang, N. Yang, H. Ye, M. Cai, L. Shen, D. Yang and T. Ren, *Scientific reports*, 2015, **5**.
28. M. Segall, P. J. Lindan, M. a. Probert, C. Pickard, P. Hasnip, S. Clark and M. Payne, *Journal of Physics: Condensed Matter*, 2002, **14**, 2717.
29. J. C. Garcia, D. B. de Lima, L. V. Assali and J. F. Justo, *The Journal of Physical Chemistry C*, 2011, **115**, 13242-13246.
30. X. Li, Y. Dai, Y. Ma, S. Han and B. Huang, *Physical Chemistry Chemical Physics*, 2014, **16**, 4230-4235.
31. P. Pyykkö and M. Atsumi, *Chemistry–A European Journal*, 2009, **15**, 186-197.
32. K. Kamiya, N. Umezawa and S. Okada, *Physical Review B*, 2011, **83**, 153413.
33. N. O. Malcolm and P. L. Popelier, *Faraday Discussions*, 2003, **124**, 353-363.
34. M. Ernzerhof, *Lecture Notes in Physics*, 2007, **500**, 60-90.
35. B. Silvi and A. Savin, *Nature*, 1994, **371**, 683-686.
36. F. Fuster and B. Silvi, *Theoretical Chemistry Accounts*, 2000, **104**, 13-21.
37. S. Noury, X. Krokidis, F. Fuster and B. Silvi, *Computers & Chemistry*, 1999, **23**, 597-604.
38. B. S. A. Savin, F. Coionna, *Canadian Journal of Chemistry*, 1996, **74**, 1088-1096.

39. Q. Liu, L. Li, Y. Li, Z. Gao, Z. Chen and J. Lu, *Journal of Physical Chemistry C*, 2012, **116**, 21556-21562.
40. M. Houssa, ., B. Broek, Van Den, E. Scalise, ., G. Pourtois, ., V. V. Afanas'Ev and A. Stesmans, . *Physical Chemistry Chemical Physics*, 2013, **15**, 3702-3705.
41. T. Qing, B. Jie, L. Yafei, Z. Zhen and C. Zhongfang, *Nanoscale*, 2014, **6**, 8624-8634.
42. N. Gao, ., J. C. Li and Q. Jiang, . *Physical Chemistry Chemical Physics*, 2014, **16**, 11673.
43. X. Chen, J. Lian and Q. Jiang, *Physical Review B*, 2012, **86**, 125437.
44. R. Yan, Q. Zhang, W. Li, I. Calizo, T. Shen, C. A. Richter, A. R. Hight-Walker, X. Liang, A. Seabaugh and D. Jena, *Applied Physics Letters*, 2012, **101**, 022105.
45. Y. Shi, K. K. Kim, A. Reina, M. Hofmann, L.-J. Li and J. Kong, *ACS nano*, 2010, **4**, 2689-2694.
46. Y.-J. Yu, Y. Zhao, S. Ryu, L. E. Brus, K. S. Kim and P. Kim, *Nano letters*, 2009, **9**, 3430-3434.
47. G. Giovannetti, ., P. A. Khomyakov, G. Brocks, ., V. M. Karpan, J. Brink, Van Den and P. J. Kelly, *Physical review letters*, 2008, **101**, 1676-1686.
48. T. Zhan, X. Shi, Y. Dai, X. Liu and J. Zi, *Journal of Physics: Condensed Matter*, 2013, **25**, 215301.
49. L. Matthes, O. Pulci and F. Bechstedt, *New Journal of Physics*, 2014, **16**, 105007.